

Dispersion in a curved tube during oscillatory flow

By M. K. SHARP†, R. D. KAMM, A. H. SHAPIRO, E. KIMMEL‡
AND G. E. KARNIADAKIS||

Fluid Mechanics Laboratory, Department of Mechanical Engineering, Massachusetts Institute of Technology, Cambridge, MA 02139, USA

(Received 11 August 1989 and in revised form 26 July 1990)

The effect of curvature on longitudinal dispersion in an axially uniform toroidal tube during oscillatory flow is investigated. The regimes of dispersion and the rate of longitudinal transport are estimated by order-of-magnitude arguments. Experiments are reported for the range, $0.66 < Dn^2/\alpha^4 < 2.4$, $5.4 < \alpha < 26$, $Sc = 0.68$, where Dn is the Dean number, α is the Womersley number and Sc is the Schmidt number. For $\beta^2 \equiv \alpha^2 Sc > 30$, curvature causes a sharp increase in the effective diffusivity, relative to that for a straight tube, by a factor of about 6 at $Dn^2/\alpha^4 \approx 2$. The results from two numerical simulation methods are also presented. One, a Monte Carlo simulation ($0.01 < Dn < 10$, $0.01 < \alpha < 0.32$, $Sc = 10^4$), predicts the spread of a bolus in quasi-steady flow. The other, a spectral-element method ($1 < Dn < 1000$, $1 < \alpha < 100$, $Sc = 0.68$), is used to find the dispersion in unsteady oscillatory flow subjected to a constant longitudinal concentration gradient. Two mechanisms are identified by which axial transport is modified by curvature. First, the enhanced lateral transport due to secondary flow decreases axial transport by a factor of up to 5 for low β^2 and increases axial transport by an even greater amount for high β^2 . Second, axial transport is enhanced owing to a form of resonance when the secondary flow circulation time is equal to the cycle period.

1. Introduction

The primary impetus for this study was the investigation of artificial respiration at high frequency, a method which has been shown to produce adequate gas exchange at tidal (breath) volumes much smaller than those characteristic of normal breathing (Drazen, Kamm & Slutsky 1984). While several mechanisms are likely to be responsible for the gas exchange observed experimentally, shear-augmented dispersion is thought to be an important factor. In this context, secondary flows generated by curvature and branching probably influence the rate of transport. Understanding the effect of curvature on dispersion in a uniform curved tube is fundamental to the study of transport in more complex geometries such as those found in the lung.

Shear-augmented dispersion in oscillatory flow has also been proposed as an alternative to heat pipes in specialized industrial applications (Kurzweg 1985). It is instrumental in the regulation of salinity, temperature, nutrients and wastes in tidal estuaries (Young, Rhines & Garrett 1982; Holley, Harleman & Fischer 1970; Fischer

† Present address: Departments of Civil and Mechanical Engineering, University of Utah, Salt Lake City, UT 84112, USA.

‡ Present address: Agriculture Engineering Department, Technion, Haifa 32000, Israel.

|| Present address: Department of Mechanical and Aerospace Engineering, Princeton University, Princeton, NJ 08544, USA.

1972; Smith 1982) and causes dispersion of biological and chemical contaminants when aquifer levels fluctuate.

Previous analytical (Watson 1983) and experimental (Joshi *et al.* 1983) studies have characterized dispersion during oscillatory flow in a straight pipe with a constant axial gradient of concentration or temperature. For these conditions, and for a given Reynolds number ($Re \equiv 2aw/\nu$, where a is the tube radius, w is the axial velocity scale and ν is the kinematic viscosity), dispersion is controlled by the ratio of radial mass diffusion time to cycle period ($\beta^2 \equiv a^2\omega/\kappa$, where ω is the radian frequency and κ the molecular diffusivity) and the Schmidt number ($Sc \equiv \nu/\kappa$).

Steady and oscillatory flow in curved tubes has been extensively studied using a variety of analytical, numerical and experimental techniques (Berger, Talbot & Yao 1983; Pedley 1980). In these, the fluid dynamic behaviour in a tube of given curvature ratio, a/b , where b is the radius of curvature, is most often characterized by the Dean number ($Dn = Re(a/b)^{\frac{1}{2}}$) for steady flow, or Dn and the Womersley number ($\alpha = \beta/Sc^{\frac{1}{2}}$) when the flow is oscillatory.

Erdogan & Chatwin (1967) used Dean's (1928) steady flow velocity profile and a perturbation method to calculate the effect of small secondary flow on dispersion, finding that the drop in axial transport correlates with the parameter Dn^2Sc . Nunge, Lin & Gill (1972) used the flow solution of Topakoglu (1967), applicable for arbitrary curvature ratio, to obtain similar results. Janssen (1976) examined larger values of Dn^2Sc using an approximate numerical method. Johnson & Kamm (1986) studied the same range of parameters but with a more accurate approach. They employed both Monte Carlo and spectral methods for low Dn using Dean's (1928) flow solution. Johnson & Kamm summarize the results of Janssen and others for the reduction in axial dispersion relative to that in a straight tube and demonstrate close agreement with experiments. These results were recently extended to higher Dn using a similar approach (Daskopoulos & Lenhoff 1988).

Eckmann & Grotberg (1987) applied a regular perturbation method valid for arbitrary curvature ratio and ratio of stroke length to tube diameter of order one to the combined problem of flow and dispersion in a curved tube during oscillatory flow. They considered the case $Sc \approx 1$ and employed boundary conditions of uniform time-averaged concentration at the ends of the tube. In their results, an abrupt increase in transport rate was observed when the ratio of stroke length to tube radius increases from about 1 to 5 for $\alpha > 5$.

In this paper, the various flow and transport regimes found during oscillatory flow in a curved tube are first established and the scaling laws for transport are obtained by employing an order-of-magnitude analysis of the governing equations along the lines of Pedley & Kamm (1988) (§2). Second, experimental results are presented for a transition region where curvature begins to affect the rate of transport (§3). Next, the results from two numerical methods are presented. In the limit of low α and low Dn the axial and secondary flow profiles are known. In §4, these are combined with a simple Monte Carlo technique to model the dispersion of a bolus of tracer material. At higher values of α and Dn , secondary flows significantly interact with and alter the axial velocity profile. For these cases, we employ a spectral-element numerical code to solve the incompressible Navier–Stokes and mass conservation equations (§5). Results from the two numerical methods and the experiments are compared and characterized (§6).

2. Order-of-magnitude analysis: asymptotic behaviour

2.1. Governing equations

The normalized momentum and mass conservation equations for fully developed laminar flow in a uniform tube of small curvature ratio (Berger *et al.* 1983) can be written in Cartesian coordinates as

$$\frac{\partial w}{\partial t} + (\mathbf{v} \cdot \nabla) w = \Pi_z + \frac{2}{Dn} \nabla^2 w, \quad (2.1)$$

$$\frac{\partial \mathbf{v}}{\partial t} + (\mathbf{v} \cdot \nabla) \mathbf{v} - w^2 \hat{\mathbf{i}} = \nabla \Pi' + \frac{2}{Dn} \nabla^2 \mathbf{v}, \quad (2.2)$$

$$\nabla \cdot \mathbf{v} = 0. \quad (2.3)$$

The species conservation equation for the same conditions is

$$\frac{\partial C}{\partial t} + (\mathbf{v} \cdot \nabla) C + wG = \frac{2}{Dn Sc} \nabla^2 C, \quad (2.4)$$

where subscript z denotes the axial derivative, and $G \equiv \partial C / \partial z$ is the constant axial concentration gradient. Also,

$$\begin{aligned} x &= \frac{\tilde{x}}{a}, & y &= \frac{\tilde{y}}{a}, & z &= \left[\frac{a}{b} \right]^{\frac{1}{2}} \frac{\tilde{z}}{a}, \\ u &= \left[\frac{b}{a} \right]^{\frac{1}{2}} \frac{\tilde{u}}{w_0}, & v &= \left[\frac{b}{a} \right]^{\frac{1}{2}} \frac{\tilde{v}}{w_0}, & w &= \frac{\tilde{w}}{w_0}, \\ t &= \left[\frac{a}{b} \right]^{\frac{1}{2}} \frac{w_0}{a} \tilde{t}, \\ p &= \frac{\tilde{p}}{\rho w_0^2} = -\Pi_z(t) z - \Pi'(x, y, t), \\ \mathbf{v} &= u \hat{\mathbf{i}} + v \hat{\mathbf{j}}, \\ \nabla &= \frac{\partial}{\partial x} \hat{\mathbf{i}} + \frac{\partial}{\partial y} \hat{\mathbf{j}}, & \nabla^2 &= \frac{\partial^2}{\partial x^2} + \frac{\partial^2}{\partial y^2}, \end{aligned}$$

where \sim denotes a dimensional variable. Note that the axial component is not included in the velocity vector so that the axial momentum equation may be treated as a passive scalar equation, allowing the simplification of solving a quasi-two-dimensional flow problem. Constraining the axial concentration gradient to be constant reduces the diffusion equation to quasi-two-dimensional form, where the axial convective term is viewed as a time-dependent 'source' term.

2.2. Term dominance criteria

Axial flow is driven by the axial pressure gradient, thus the pressure term in (2.1) may be balanced by unsteady, convective or viscous terms (or some combination of these). Similarly, flow in the cross-sectional plane is driven by centrifugal forces and may be dominated by unsteady, convective or viscous terms (see (2.2)). Asymptotic regimes of flow are identified by forming ratios among the unsteady, convective and viscous terms with the following characterizations: $\tilde{t} \sim T$ (cycle period), $\tilde{w} \sim w_0$ (bulk r.m.s. velocity), $\tilde{u}, \tilde{v} \sim v_s$ (the characteristic secondary flow velocity) and $\tilde{x}, \tilde{y} \sim a$.

The dominance criteria obtained from the cross-sectional momentum equations are found to be identical to those obtained from the axial momentum equation. Both, however, require scaling estimates for the secondary flow velocity which may be obtained by balancing the dominant term in the cross-sectional momentum equations with the centrifugal term, obtaining for viscous-dominated flow

$$\frac{v_s}{w_0} \sim \left[\frac{a}{b} \right]^{\frac{1}{2}} Dn, \quad (2.5)$$

for flow dominated by unsteadiness

$$\frac{v_s}{w_0} \sim \left[\frac{a}{b} \right]^{\frac{1}{2}} \frac{Dn}{\alpha^2}, \quad (2.6)$$

and for flow dominated by convective effects

$$\frac{v_s}{w_0} \sim \left[\frac{a}{b} \right]^{\frac{1}{2}}, \quad (2.7)$$

where (2.7) presumes that the core flow is not inviscid. The more correct limit for large Dn , taking account of the rotational but inviscid core, modifies the right-hand side of (2.7) by a factor $Dn^{-\frac{1}{2}}$ (Pedley 1980). For the purpose of defining flow regimes, however, (2.7) will suffice.

Using (2.5)–(2.7), dominance criteria may be established which are consistent with these scalings and conform to the asymptotic regimes found by Yamane *et al.* (1985), i.e. flow is viscous when the viscous terms in (2.1) and (2.2) dominate their respective unsteady and convective terms, or when

$$\alpha^2 \ll 1 \quad \text{and} \quad Dn \ll 1 \quad (\text{zones 1, 2, 4 on figure 1 } a, b), \quad (2.8)$$

flow is unsteady when the unsteady terms dominate the viscous and convective terms,

$$\alpha^2 \gg 1 \quad \text{and} \quad Dn/\alpha^2 \ll 1 \quad (\text{zone 3}), \quad (2.9)$$

and flow is convective when the convective terms are much larger than the unsteady and viscous terms,

$$Dn/\alpha^2 \gg 1 \quad \text{and} \quad Dn \gg 1 \quad (\text{zone 5}). \quad (2.10)$$

These regimes are indicated on figure 1 (*a, b*) for two values of Sc .

Similarly, species transport in the axial direction is driven by axial convection, thus dispersion may be unsteady, convective (in the lateral sense) or diffusive (i.e. molecular diffusion dominates) depending on the relative magnitudes of the corresponding terms in (2.4). The dominance criterion depends on the type of flow because of the different scaling (2.5)–(2.7) for secondary flow. For viscous flow, dispersion is diffusive when the diffusive term dominates the unsteady and convective terms,

$$\beta^2 \ll 1 \quad \text{and} \quad Dn^2 Sc \ll 1 \quad (\text{zone 1}), \quad (2.11)$$

dispersion is unsteady when the convective and diffusive terms are small,

$$\frac{Dn^2}{\alpha^2} \ll 1 \quad \text{and} \quad \beta^2 \gg 1 \quad (\text{zone 2}), \quad (2.12)$$

and dispersion is convective when unsteady and diffusive terms are small,

$$\frac{Dn^2}{\alpha^2} \gg 1 \quad \text{and} \quad Dn^2 Sc \gg 1 \quad (\text{zone 4}). \quad (2.13)$$

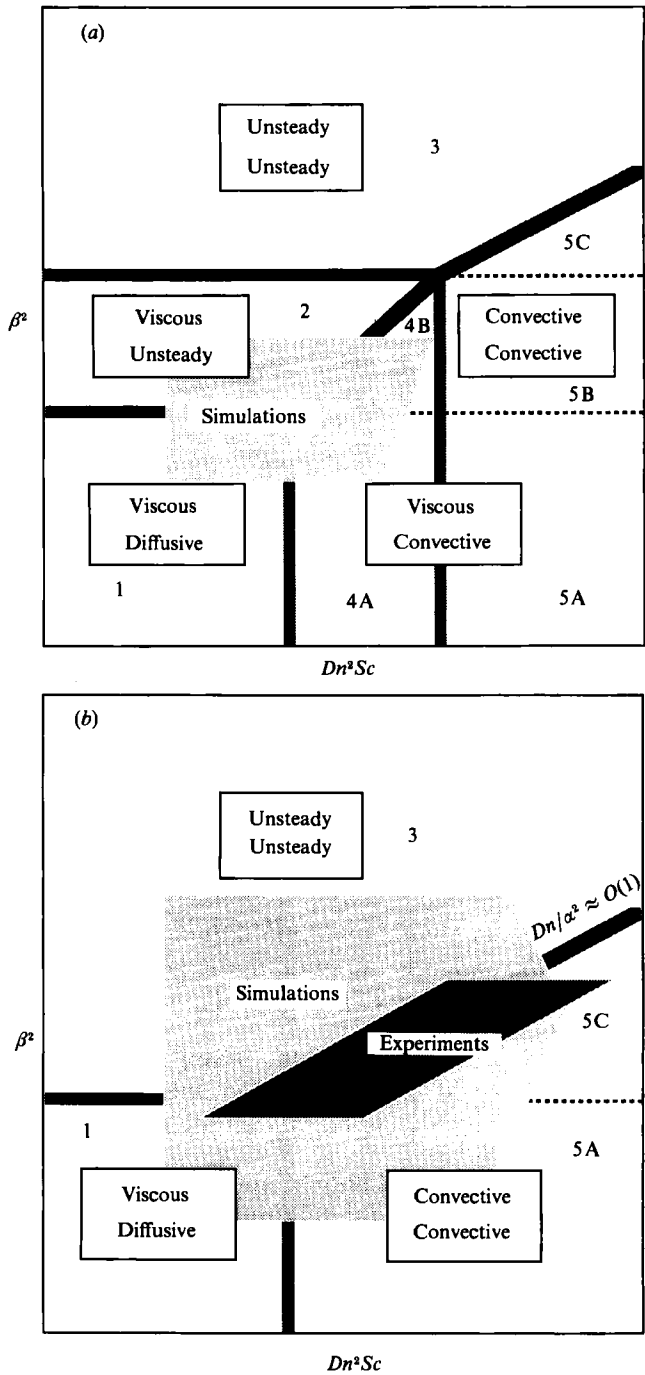


FIGURE 1. Mapping of different transport regimes as determined by scaling arguments. Indicated in each box are the dominant term in the momentum (top) and transport (bottom) equations for each zone. (a) For $Sc \geq 1$, (b) $Sc = 1$.

The analysis reveals that, for $Sc \geq 1$ (as is generally the case), dispersion must be unsteady when the flow is unsteady and dispersion must be convective when the flow is convective. Thus the criteria for unsteady flow and dispersion (zone 3) are given by (2.9) and the criteria for convective flow and dispersion (zone 5) are given by (2.10). These two zones are common to figures 1(a) and 1(b).

For most gases, $Sc \approx 1$ and all transitions between the asymptotic dispersion regimes coincide with those between the flow regimes. In this case, zones 2 and 4 are eliminated and the criteria for viscous flow and diffusive dispersion (zone 1) are given by (2.8).

2.3. Order of magnitude estimates for transport rate

An expression for the effective diffusivity can be developed from a statistical perspective (Taylor 1921). Neglecting axial molecular diffusion:

$$D_{\text{eff}} = \frac{1}{A} \int_A \int_0^\infty \langle \tilde{w}(0) \tilde{w}(\tilde{t}) \rangle d\tilde{t} dA, \quad (2.14)$$

where $\langle \rangle$ denotes an ensemble average. Pedley & Kamm (1988) employed (2.14) to study the character of axial transport as embodied in a dimensionless transport coefficient \mathcal{D} , defined by

$$\mathcal{D} = D_{\text{eff}}/w_0^2 T, \quad (2.15)$$

where T is the cycle period. Following their rationale, the contribution of longitudinal molecular diffusion is assumed to be additive and the time integral is approximated by $w_{\text{rel}}^2 t_c$, where w_{rel} is the characteristic axial velocity of species particles relative to the average (an average over the area occupied by particles in relative motion) and t_c is the time during which the velocity of a fluid particle remains correlated. Accordingly, the denominator of (2.15) may be thought of as the scale for D_{eff} when the relative velocity takes on its maximum value, w_0 , and the particle motions remain correlated for a time T . The area integral is represented by including a factor, F_A , characterizing the fraction of the cross-sectional area occupied by the particles travelling at speed w_{rel} . With these approximations, \mathcal{D} is expressed as

$$\mathcal{D} \approx \left(\frac{w_{\text{rel}}}{w_0} \right)^2 \frac{t_c}{T} F_A. \quad (2.16)$$

This approach was used by Pedley & Kamm (1988) to predict the rates of axial dispersion in an annular region with prescribed secondary and axial velocity distributions as a model for curved-tube flow. This same approach is applied below to the zones defined in §2.2.

Viscous-dominated flow, diffusion-dominated dispersion (zone 1). This zone corresponds to the straight-tube, quasi-steady result of Taylor (1953). The result obtained by Pedley & Kamm (1988) from (2.16) using $w_{\text{rel}} = w_0$, $t_c = a^2/\kappa$ and $F_A = 1$ gives

$$\mathcal{D} \sim \beta^2 \quad (2.17)$$

for limits (2.11).

Viscous flow, low- β convective dispersion (zone 4a). As Dn increases, secondary flows begin to produce effective convective mixing over the tube cross-section. The influence of secondary flow on dispersion is characterized by the ratio of the convective and diffusive terms in (2.4) (the ratio of radial diffusion time, τ_{rd} , to secondary flow time, τ_s):

$$\frac{\tau_{\text{rd}}}{\tau_s} \sim Dn^2 Sc, \quad (2.18)$$

as in the steady flow case. This ratio is simply the secondary flow Péclet number (Rhines & Young 1983). As Dn^2Sc increases in magnitude, lateral convective mixing causes a reduction in axial transport. Owing, however, to the constancy of the secondary flow streamline pattern for small Dn , convective mixing only tends to smooth out concentration gradients *along* each secondary flow streamline. Therefore, the maximum possible effect of secondary flow is to cause the concentration isopleths (lines of constant concentration) and secondary flow streamlines to coincide. This occurs on a timescale $\tau_e \sim (av_s/\kappa)^{1/2}a/v_s$ (Rhines & Young 1983) where a is taken to be the characteristic dimension of the velocity shear field, or when

$$\frac{\tau_e}{\tau_{rd}} \sim (Dn^2Sc)^{-2/3} \ll 1. \quad (2.19)$$

In this limit, dispersion is controlled by diffusion across secondary flow streamlines. With equilibration of concentration along the streamline, the characteristic axial velocity of a particle on a particular streamline may be represented by the streamline average (the integral along the streamline of the axial velocity weighted by the inverse of the streamwise velocity). Although the streamline average velocity profile is not readily characterized by inspection, Johnson & Kamm (1986) calculated the profile from Dean's perturbation solution and found that the effect of mixing along secondary flow streamlines accounts for 75% of the observed reduction in D_{eff} and that the character of \mathcal{D} for $Dn^2Sc > 10^5$ is the same as that found in a straight tube; that is, $\mathcal{D} \sim \beta^2$. This result applies for $\beta \ll 1$ and limits (2.13).

Viscous flow, unsteady dispersion (zone 2). A fundamental difference exists between species transport in steady as opposed to oscillatory flow. In steady flow, axial transport is maximized when $\kappa = 0$; fluid particles move purely by convection at the local fluid velocity. In oscillatory flow with $\kappa = 0$, species particles move periodically about their original position, never achieving any transport in the cycle-average sense. Thus, for oscillatory motion with zero mean, lateral mixing of some kind is essential for longitudinal transport to occur at all. Furthermore, it will be shown that a maximum in transport rate is achieved when the diffusion time and cycle period coincide or when $\beta \sim O(1)$.

Secondary flow induced by tube curvature causes lateral mixing supplemental to transverse diffusion. Thus, longitudinal transport is reduced by secondary currents for steady flow and low- β oscillatory flow because the transverse mixing time is already smaller than the optimum. For high β , longitudinal transport is increased because secondary flow reduces the 'greater-than-optimal' transverse mixing time.

Since the effects of curvature are negligible in zone 2 ($Dn^2/\alpha^2 \ll 1$), the result for oscillatory flow in a straight tube pertains (Watson 1983). Noting that $t_c \sim T$ and $w_{\text{rel}} \sim (w_0/a)(\kappa T)^{1/2}$, we obtain

$$\mathcal{D} \sim \beta^{-2} \quad (2.20)$$

which applies when limits (2.12) are satisfied.

Viscous flow, high- β convective dispersion (zone 4b). The parameter that characterizes the relative effect on dispersion of convection and unsteadiness is the ratio of the convective and unsteady terms in (2.4):

$$\frac{T}{\tau_s} \sim \frac{v_s T}{a} \sim \frac{Dn^2}{\alpha^2}. \quad (2.21)$$

Since $Dn^2/\alpha^2 > O(10)$ in zone 4b, the effects of secondary flow are significant.

According to the reasoning presented for zone 2, secondary flow is expected to cause \mathcal{D} to increase. The amount of increase, however, is limited to that observed when the concentration isopleths and secondary flow streamlines coincide (as in zone 4a). In this limit (for sufficiently large Dn^2/α^2), $t_c \sim T$ and $w_{rel} \sim (w_0/a)(\kappa T)^{\frac{1}{2}}$, yielding

$$\mathcal{D} \sim \beta^{-2}. \quad (2.22)$$

This result applies for $\beta \gg 1$ and limits (2.13).

Unsteady flow, unsteady dispersion (zone 3). The influence of secondary flow is characterized by the ratio of the convective and unsteady terms in (2.4):

$$\frac{T}{\tau_s} \sim \frac{v_s T}{a} \sim \frac{Dn^2}{\alpha^4}. \quad (2.23)$$

Since $Dn^2/\alpha^2 \ll 1$ in zone 3, the effects of secondary flow are small, thus

$$\mathcal{D} \sim \beta^{-1} Sc^{-\frac{1}{2}} \quad (2.24)$$

which applies for limits (2.9).

Convective flow, convective dispersion (zone 5). The nature of transport in this regime is more complex owing to the effect that secondary flow exerts on the axial profile, in contrast to the entire region of viscous-dominated flow where the axial velocity field is unaffected. In addition, the secondary flow streamlines are changing during the course of the oscillation cycle. All this makes prediction of the scaling laws for dispersion difficult. However, analogous to the zone 2–4b transition, one might expect the additional mixing induced by secondary flow to increase axial transport since β is large.

Convective resonance. When the time, $\tau_s \sim av_s$, required for a fluid particle to traverse the secondary flow circuit equals the cycle period, T , a resonant condition can exist as demonstrated in the model problem studied by Pedley & Kamm (1988). As the particle circulates between regions of high and low axial velocity during each cycle, it could, for instance, travel at a speed faster than the average axial velocity on the forward stroke and slower than average on the receding stroke, achieving a net axial displacement over each cycle. Such resonance exists when $\tau_s \sim nT$ where n is an odd integer, although the displacement rate diminishes with increasing n . While less obvious, it can be shown that all streamlines may exhibit some degree of ‘resonance’ (Pedley & Kamm 1988).

Particles on the primary resonant streamline ($n = 1$) have the secondary velocity $v_{cr} = l_s/T$, where l_s is the streamline circumference. Particles on this streamline will be displaced some axial distance each cycle; the characteristic axial velocity of motion will scale with w_0 . The axial direction of travel on each cycle will be correlated over the time it takes that fluid particle to migrate to the opposite side of the same streamline and hence become ‘antiresonant’. Owing to the influence of shear-augmented diffusion, the timescale for antiresonance to occur is τ_e , as described earlier. During this period, a region surrounding the resonant streamline is involved encompassing a band of width

$$\delta_{cr} \sim \left[\frac{\kappa l_s}{\partial v_s / \partial n} \right]^{\frac{1}{3}}, \quad (2.25)$$

where $\partial v_s / \partial n$ is the characteristic gradient in secondary velocity normal to the secondary flow streamline. Combining these estimates with (2.15) we obtain

$$\mathcal{D} \sim \text{constant}, \quad (2.26)$$

assuming that $l_s \sim a$ and $\partial v_s / \partial n \sim v_s/a$.

The regions where the potential for convective resonance exists are along the boundaries of the convective dispersion regimes: for $Dn^2/\alpha^2 = \text{const.}$ for the zone 2–4*b* transition, and $Dn^2/\alpha^4 = \text{const.}$ for the zone 3–5*c* transition. The first of these two boundary zones matches the description just given: for viscous-dominated flow the secondary flow streamline pattern remains constant throughout a flow cycle and the only mechanism by which a fluid particle can migrate from a resonant to antiresonant condition is by diffusion. Hence, dispersion should follow (2.26).

The transition at constant Dn^2/α^4 is more difficult to characterize, again because of the coupling between the secondary flow and the axial velocity profile. The complexity of this interaction is seen in the numerical results presented later. By analogy to the convective resonance zone found in the viscous flow regime, an increase in axial transport is anticipated. The magnitude of this increase, however, will be reduced by the tendency for mixing across secondary flow streamlines due to the changing streamline pattern.

3. Experiments

3.1. Rationale

To determine D_{eff} experimentally, a transient method was devised involving the progressive spread of an initial discontinuity in concentration given by

$$\begin{aligned} C(\tilde{z}, \tilde{x}, \tilde{y}, \tilde{t} = 0) &= C_0 \quad \text{for } \tilde{z} < 0, \\ C(\tilde{z}, \tilde{x}, \tilde{y}, \tilde{t} = 0) &= 0 \quad \text{for } \tilde{z} > 0. \end{aligned}$$

The rate of spread of this discontinuity can be described by an effective axial diffusivity, D_{eff} , obtained by transforming (2.4) to a reference frame moving with the mean fluid velocity (ζ is the axial coordinate in the moving reference frame) and integrating over the tube cross-sectional area, A :

$$D_{\text{eff}} = \frac{\frac{1}{A} \int_A \left(w' C' + \kappa \frac{\partial C}{\partial \zeta} \right) dA}{\frac{\partial \bar{C}}{\partial \zeta}}. \quad (3.1)$$

The velocity and concentration are each expressed as the sum of the respective cross-sectional average (\bar{w} , \bar{C}) and deviation from the average (w' , C'). Assuming D_{eff} to be a function of time only, the one-dimensional diffusion equation is obtained:

$$\frac{\partial \bar{C}}{\partial \tilde{t}} = D_{\text{eff}}(\tilde{t}) \frac{\partial^2 \bar{C}}{\partial \zeta^2}. \quad (3.2)$$

The solution to (3.2) with these initial conditions for a time-dependent diffusivity is found using a time transformation (Crank 1956):

$$\left. \begin{aligned} \frac{\bar{C}}{C_0} &= \frac{1}{2} \text{erfc}(\eta), \\ \eta &= \frac{\zeta}{2(\tilde{t} D_{\text{eff}})^{\frac{1}{2}}}, \end{aligned} \right\} \quad (3.3)$$

where $\overline{D_{\text{eff}}}$ is the effective diffusivity averaged from 0 to t . Thus, measurements of

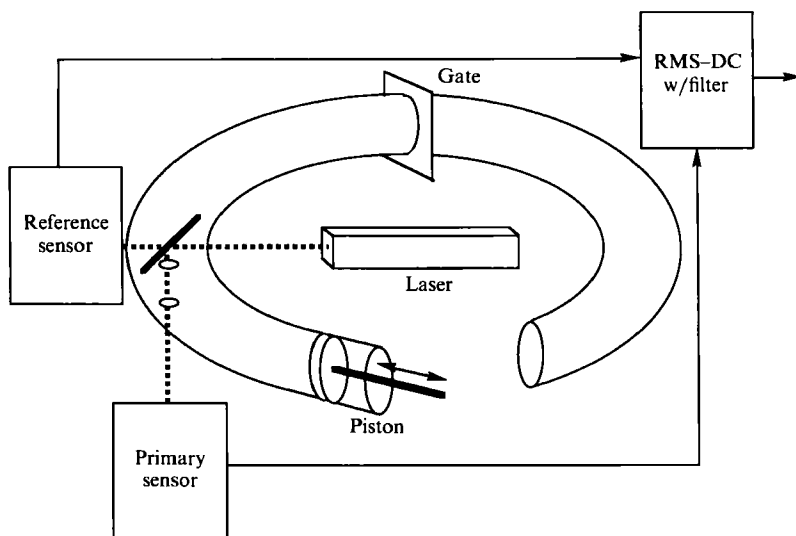


FIGURE 2. Sketch of experimental apparatus.

\bar{C} at a fixed location z_0 can, in principle, be used to calculate $\overline{D_{\text{eff}}}$. Note that since D_{eff} is periodic on time $\frac{1}{2}T$, $\overline{D_{\text{eff}}}$ is constant for $\tilde{t} = \frac{1}{2}nT$.

A difficulty arises, however, in that the measurement method employed yields values for the diametrical-average concentration (C_d), rather than \bar{C} . To motivate the method of analysis used in this study, consider the concentration distribution at mid-cycle on two consecutive half-cycles. From considerations of symmetry, it can be seen that the cross-sectional concentration distributions are essentially reversed; that is, if the concentration in the core is higher than near the wall on the forward stroke, this relationship will be inverted (it will be lower in the core) on the reverse stroke. The sign of the difference $C_d - \bar{C}$ will therefore alternate once each half-cycle. Consequently, if values for η , and then $\overline{D_{\text{eff}}}$, are computed for each value of C_d , the calculated $\overline{D_{\text{eff}}}$ values will alternately fall above and below the correct value that would have been computed from \bar{C} . This antisymmetry suggests that a more accurate estimate for $\overline{D_{\text{eff}}}$ might be obtained by averaging the values for $\overline{D_{\text{eff}}}$ calculated on successive half-cycles using C_d (call this $\overline{D_{\text{eff},d}}$) and fitting them to the equation

$$(\overline{D_{\text{eff},d}} \tilde{t})_k + (\overline{D_{\text{eff},d}} \tilde{t})_{k+1} = \overline{D_{\text{eff}}} \tilde{t}_k + \overline{D_{\text{eff}}} (\tilde{t}_k + \frac{1}{2}T) + B, \quad (3.4)$$

where the constant B is added to account for the start-up transient. The validity of this approach was confirmed by initial tests in a straight-tube system and by spectral-element calculations for a curved tube with linear variation in mean concentration (Sharp 1987).

3.2. Apparatus

The experiments were performed in a curved-tube apparatus (figure 2) formed from half-circular 2.54 cm diameter channels of 58.4 cm radius of curvature machined into two 2.54 cm thick sheets of acrylic. A 30° wedge was cut away to allow attachment of a piston at one end of the torus and a flexible polyethylene bag at the other. The torus, though limited in length, avoided any potential effects due to a helix angle. Entrance effects in oscillatory flow are confined to a region extending roughly one stroke length from each end; for these experiments, a maximum of 15 radii.

At the midpoint in the torus was located a thin sheet of stainless steel sealed by

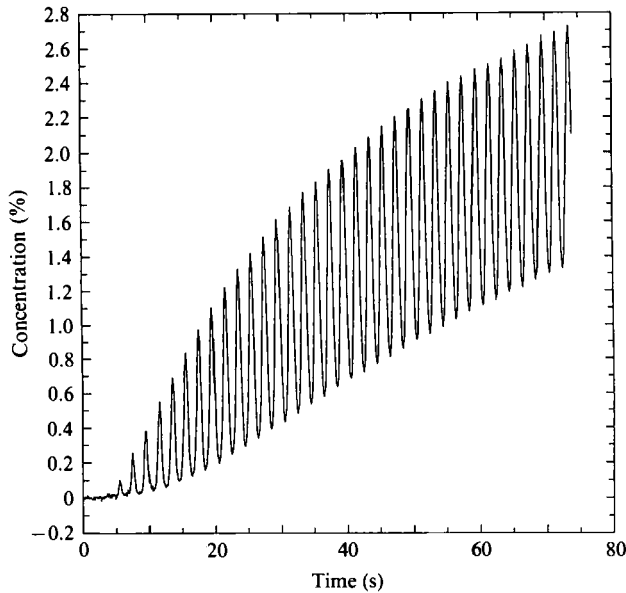


FIGURE 3. One sample of the raw experimental data ($\alpha = 5.81$, $Dn^2/\alpha^4 = 0.893$) in the form of tracer concentration *vs.* time.

rubber O-rings to produce a removable gate. The gate was inserted initially to produce a discontinuity in gas composition, 11% methane in nitrogen on one side and 5% helium in nitrogen, neutrally buoyant with the methane mixture, on the other.

At the start of an experiment, the gate was removed and the piston motion started. The fluctuations in methane concentration were measured at a single location by a laser absorption technique which yields a measure of the average concentration of tracer across the tube diameter, the details of which are provided by Joshi *et al.* (1983). One of two measurement sites was used, 10 or 20 cm from the gate. Data were obtained from the first 38 cycles at a rate of 40 times per cycle and recorded by a DEC MINC-23 computer.

An example raw data set is shown in figure 3 in terms of diametrical-average concentration as a function of time. As expected, a short time passes before the concentration at the measurement site rises above zero. Subsequently, the mean value and amplitude of the concentration fluctuations increase, the mean value ultimately approaching the mean of the two initial concentrations. The amplitude eventually falls toward zero as the concentration gradient becomes progressively smaller.

In separate experiments, the transition to turbulence was studied by two different methods. One approach was simply to look for the first appearance of random fluctuations in the tracer concentration traces. The other involved the use of a hot-film probe (TSI model 1201-60) positioned 0.32 cm from the tube wall. The use of these methods to measure turbulence is described in §3.4.

3.3. Results: dispersion

Experiments were conducted at 16 frequencies ($2 < \beta^2 < 500$) and 6 stroke lengths, L , corresponding to six different values of $Dn^2/\alpha^4 \sim (a/b)(L/a)^2$, namely 0.658, 0.893, 1.30, 1.59, 1.80, 2.37. Here, and in subsequent sections, Dn is computed using the

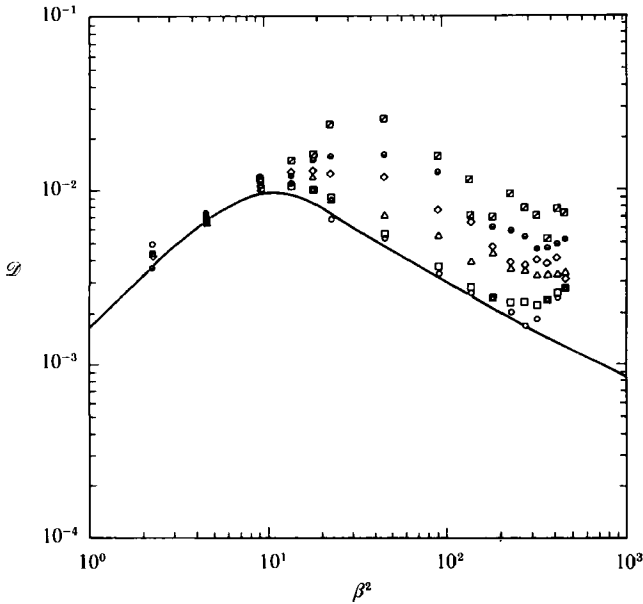


FIGURE 4. Experimental results for normalized diffusivity \mathcal{D} plotted against β^2 . Solid line: theoretical prediction for straight tube (Watson 1983). \circ , $Dn^2/\alpha^4 = 0.658$; \square , 0.893; \triangle , 1.30; \diamond , 1.59; \ominus , 1.80; \boxtimes , 2.37.

bulk r.m.s. velocity. The experiments span the three low- Dn flow regimes of Yamane *et al.* (1985) and lie in zones 1, 3 and 5 in figure 1 (*b*). The Schmidt number for all runs was 0.68.

The results of the midcycle-average regression for the cycle average effective diffusivity, $\overline{D_{\text{eff}}}$, are shown in figure 4 in terms of the dimensionless transport coefficient; the solid line represents the theoretical solution for oscillatory flow in a straight tube (Watson 1983) whereas the symbols represent different values of Dn^2/α^4 . The viscous flow results for $\beta^2 < 10$ coincide with the straight-tube theoretical prediction, except at the lowest frequency, where the enhancement for the smallest value of Dn^2/α^4 is only about twice the molecular diffusivity; here, experimental errors due to flow disturbances or buoyancy effects represent much larger relative errors than for the higher- β results. Except for the highest frequencies, values of \mathcal{D} for $Dn^2/\alpha^4 < 1$ fall on or just above the straight-tube theoretical prediction, as would be expected from the flow regime (figure 1*b*). For $\beta^2 \gtrsim 20$, \mathcal{D} increases abruptly when Dn^2/α^4 exceeds unity, but an upper limit in the dispersion enhancement is not discernible. This upper limit could not be investigated with the present experimental system because of stroke length constraints; however, the spectral-element simulations of §5 revealed that the experiments at the highest Dn^2/α^4 were near a maximum in \mathcal{D} .

The abrupt increase in transport rate observed as Dn^2/α^4 increases above about 1 corresponds to the enhancement predicted by Eckmann & Grotberg (1987), suggesting a common mechanism. These similarities are discussed further in §6.

The reason for the upturn in \mathcal{D} at high frequency for the two smallest stroke lengths is not clear. The increase in the enhancement relative to that for a straight tube seen in these two data sets is consistent with the enhanced lateral mixing that turbulence would produce. Of course, the other data sets at larger Dn^2/α^4 would also

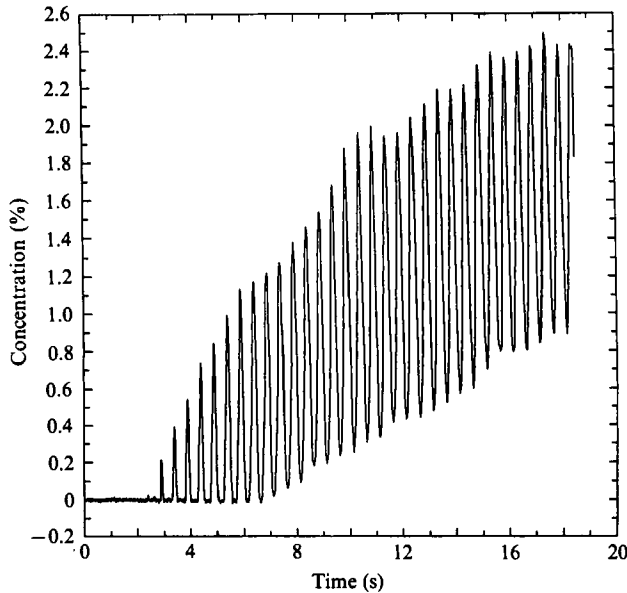


FIGURE 5. Data for concentration *vs.* time for $\alpha = 12$, $Re/\alpha = 90$ showing the effect of apparent turbulence. Compare to figure 3.

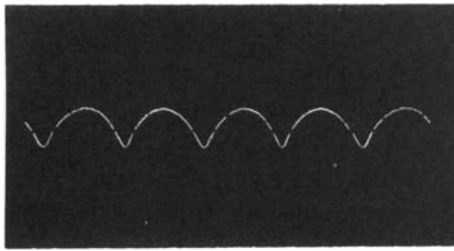
be influenced by turbulence, but the extra lateral mixing appears to have less of an effect on axial transport, possibly because the lateral mixing is already enhanced owing to secondary flow.

3.4. Results: turbulence

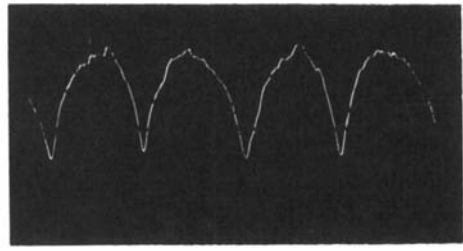
Random fluctuations in concentration were noticed in several experiments. The fluctuations were of the order of a few percent at the onset and grew in characteristic frequency and amplitude as piston frequency and/or stroke length increased (an example of the more severe fluctuations is shown in figure 5). The occurrence of fluctuations correlated well with the Reynolds number based on Stokes layer thickness, Re/α , with the transition region being approximately $70 < Re/\alpha < 120$. Similar fluctuations were not apparent in the straight-tube experiments (Sharp 1987), even though they reached higher values of Re/α .

To further investigate this phenomenon, a hot-film probe was inserted into the tube at mid-length and at radial position, $r/a = 0.75$. The velocity traces obtained (see for example, figure 6) suggest a transition in the range $80 < Re/\alpha < 130$. In both cases, a transition to turbulence is observed at values of Re/α well below the previously reported transition at $Re/\alpha \approx 550$ to large-amplitude turbulence in oscillatory flow in a straight tube (Hino, Sawamoto & Takasu 1976).

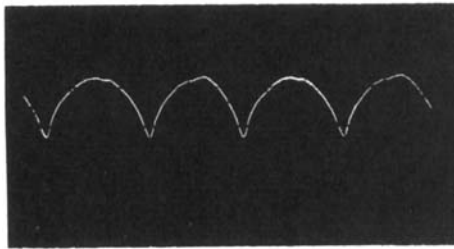
This result is puzzling for several reasons. First, other experiments have demonstrated that, for steady flow, curvature tends to boost the transition Reynolds number (Sreenivasan & Strykowski 1983). Second, the transition to turbulence in oscillatory flow in a straight tube is characterized by the appearance, then rapid dissipation, of turbulent bursts that appear just as the flow begins to decelerate. In contrast, the disturbances in the curved tube are observed during the period of peak velocity, both during acceleration and deceleration, and lack the abrupt, almost explosive character seen in straight tubes. The instabilities seen here could be associated with a much smaller-amplitude disturbance seen in straight tubes at



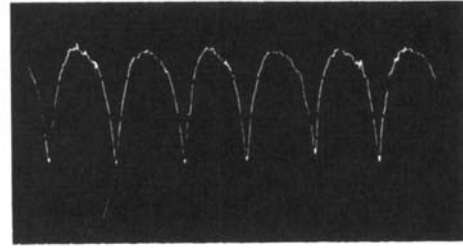
$\alpha = 5.81, Re/\alpha = 60.7$



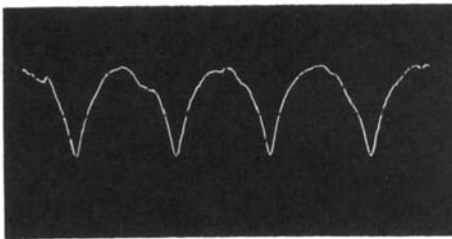
$\alpha = 16.4, Re/\alpha = 172$



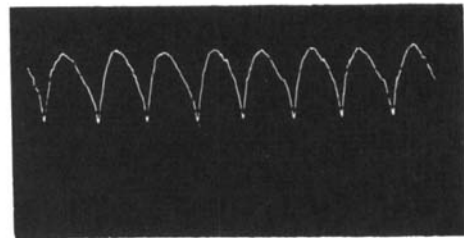
$\alpha = 8.22, Re/\alpha = 85.8$



$\alpha = 20.1, Re/\alpha = 210$



$\alpha = 11.6, Re/\alpha = 121$



$\alpha = 23.2, Re/\alpha = 243$

FIGURE 6. Traces from the hot-film probe showing the variation in velocity with time at a location 0.32 cm from the tube wall. All data for $L/a = 14.75$.

somewhat lower values of Re/α (about 180 for the experiments of Hino *et al.* 1976). These small-amplitude disturbances observed in straight tubes, however, are typically confined to the early stages of flow acceleration and are of a much smaller amplitude than those observed here.

Finally, while it is possible that the presence of the flow probe may have contributed to the instability in those experiments, the fact that fluctuations were evident in the concentration measurements as well proves that disturbances do occur even in the absence of a probe.

The unique character of the instability seen in these curved-tube experiments raises the possibility that an entirely different mechanism may be responsible, perhaps one linked to the presence of secondary flows. Further tests or analyses will be needed, however, to adequately address this issue.

4. Monte Carlo simulations

4.1. Methods

The model, adapted from Johnson & Kamm (1986), is a probabilistic treatment of longitudinal dispersion of a number of tracer 'particles'. The Lagrangian displacement of each particle was tracked by sequentially advancing (1) in the Poiseuille axial flow field, (2) in the Dean (1928) secondary flow field and (3) in a random walk dispersive displacement. Particle displacements were computed by the Euler-forward-differencing scheme, except for (2) which was by a method of second-order accuracy. The effective diffusivity was derived from the rate of change of the variance of the tracer cloud.

Different aspects of the model restricted the range of validity of the results. The momentum equation used by Dean (1928) to solve for the secondary velocity field applies only for curvature ratio $a/b \ll 1$. The first term of his expansion for the secondary flow stream function used in the simulations is restricted to $Dn < 17$ and strictly applies only to quasi-steady flow, $\alpha < O(1)$. Since Johnson & Kamm (1986) found that the effective axial diffusivity, D_{eff} , is predominantly influenced by the enhanced cross-sectional mixing due to secondary flow and virtually unaffected by the associated shift in the axial velocity profile, the latter was not included.

The explicit differencing scheme dictated time-step constraints identical to those discussed by Johnson & Kamm related to radial diffusion time, secondary flow time and numerical diffusion time. In addition, the time step was constrained to be much less than the cycle period, $\Delta t < \frac{1}{40}T$. In order to sample a wide range of β^2 and maintain α small, it was necessary to set the Schmidt number to a large value ($Sc = 10^4$), which is typical of solute dispersion in liquids. The number of particles was 500 in all runs. The expected error in D_{eff} scales as $N_p^{-\frac{1}{2}}$, where N_p is the number of particles.

From an initial condition of particles randomly distributed on a cross-sectional plane, the simulation was run for two cycles and the axial dispersion was computed at the end of each cycle. No systematic differences were found between the values for D_{eff} computed on the first two cycles, suggesting that a periodic steady state is set up almost immediately, even when $\beta^2 > O(1)$.

4.2. Monte Carlo results

A matrix of calculations was performed covering the ranges $1 < Dn^2Sc < 10^6$ and $1 < \beta^2 < 10^3$ (spanning zones 1, 2 and 4), except for the region of low β^2 and high Dn^2Sc where computational time became excessive. The dimensionless dispersion coefficient, \mathcal{D} , is plotted as a function of Dn^2Sc in figure 7(a) and against Dn^2/α^2 in figure 7(b). Several limits are evident in the results. First, dispersion in a curved tube is indistinguishable from that in a straight tube when the characteristic secondary flow time is either long compared to the radial diffusion time ($Dn^2Sc \gtrsim 100$) for low β^2 , or is long compared to the cycle period ($Dn^2/\alpha^2 \gtrsim 10$) for high β^2 . The curvature effect at low β^2 can be seen in the curves for $\beta^2 = 1$ and 10. These are in close agreement with the steady flow prediction of Johnson & Kamm (1986); hence, steady flow behaviour is observed for all values of Dn^2Sc when $\beta^2 \lesssim 10$. In this quasi-steady limit, \mathcal{D} is diminished owing to curvature by a limiting factor of about 5 at high Dn^2Sc . The diminution continues as β increases until $\beta^2 \approx 50$; above this, mixing due to secondary flow enhances \mathcal{D} and, for a certain range of Dn^2/α^2 , curved-tube dispersion exceeds that in a straight tube (figure 7b). The curves for $\beta^2 = 10^2$ and 10^3 show clear maxima at $Dn^2Sc = 10^4$ and 10^5 , respectively (figure 7a), or, when $Dn^2/\alpha^2 \approx 10^2$

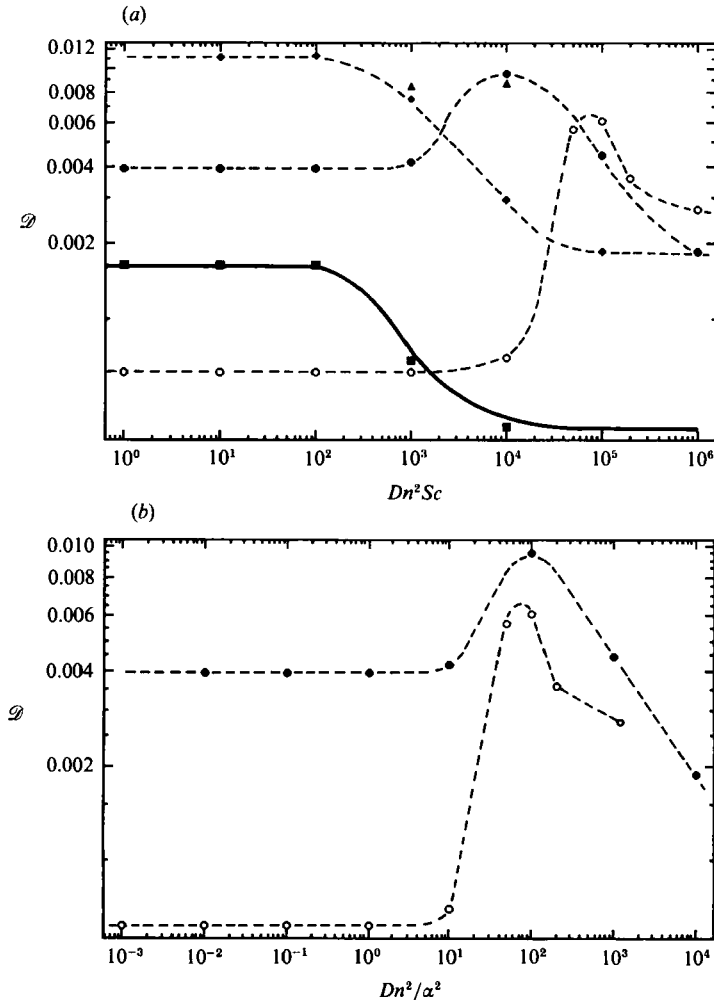


FIGURE 7. Results from the Monte Carlo simulation, $Sc = 10^4$. (a) \mathcal{D} vs. $Dn^2 Sc$. Symbols denote values of β^2 : \blacksquare , 1; \blacklozenge , 10; \blacktriangle , 50; \bullet , 100; \circ , 1000. Solid line is the prediction for steady curved-tube flow of Johnson & Kamm (1986). Dashed lines are drawn to fit the present data. (b) \mathcal{D} vs. Dn^2 / α^2 . Symbols as in (a).

(figure 7b). As pointed out in §2, Dn^2 / α^2 represents a ratio of secondary flow time to cycle time and the appearance of a peak when $Dn^2 / \alpha^2 = \text{constant}$ is strongly suggestive of convective resonance. According to the previous scaling predictions, convective resonance causes \mathcal{D} to remain constant near its maximum value, consistent with these results. Our results in zone 4b are too sparse to either confirm or disprove the scaling predictions of §2.

5. Spectral-element simulations

Numerical simulations of dispersion along a constant axial concentration gradient (see the Appendix for methods) were performed at six values of β^2 between 1 and 10^3 . The Schmidt number for all runs was 0.68 as in the experiments; values of $Dn^2 Sc$ for each test sequence at constant β^2 are contained in the approximate range

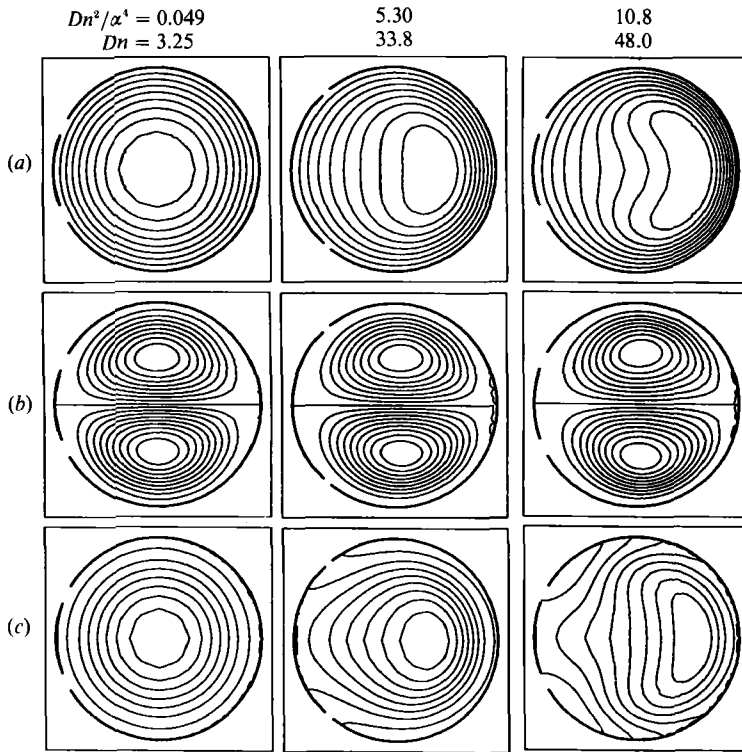


FIGURE 8. Contour plots showing the spectral-element results for different values of Dn . $\beta^2 = 10$, $Sc = 0.68$, ϕ (phase angle) = 90° . Shown, from top to bottom, are (a) axial velocity, (b) secondary flow streamlines and (c) concentration isopleths. Dashed lines on the axial velocity plots indicate negative velocity and, on the concentration plots, indicate concentration lower than the cycle average. The centre of curvature is to the left.

$1 < Dn^2 Sc < 10^5$. The results are discussed below, grouped in terms of the values of β^2 for each run and are presented in figures 8–12. In §6 the predicted rates of axial dispersion are discussed in the context of the Monte Carlo simulations and the experiments.

$\beta^2 = 1$. The behaviour at low frequency was essentially indistinguishable from that in steady flow. The effects of curvature on axial velocity profiles set in at $Dn \approx 10$; on concentration at $Dn^2 Sc \approx 10^2$.

$\beta^2 = 10$. Detailed results for this sequence of simulations are presented in figures 8 and 9. As Dn increases, the axial velocity and concentration distributions are at first axisymmetric (e.g. $Dn = 3.25$), then become increasingly skewed along the axis of curvature, with peaks approaching the outer wall. The secondary flow streamline pattern remains relatively fixed as flow conditions vary. At the highest values of Dn , there is a tendency for the peak in axial velocity to form near the inner wall of the bend as the flow begins to accelerate (following inviscid behaviour), then to move progressively towards the outside wall, convected there by the secondary motions. There is some suggestion that, at higher values of Dn , the axial velocity peak will separate into two, symmetric about the plane of curvature, as seen at $\beta^2 = 100$. The peak in axial velocity lags the pressure gradient by an amount ranging from 63.3° to 55.9° as Dn increases. The time-dependent volume flow rate is indistinguishable from sinusoidal.

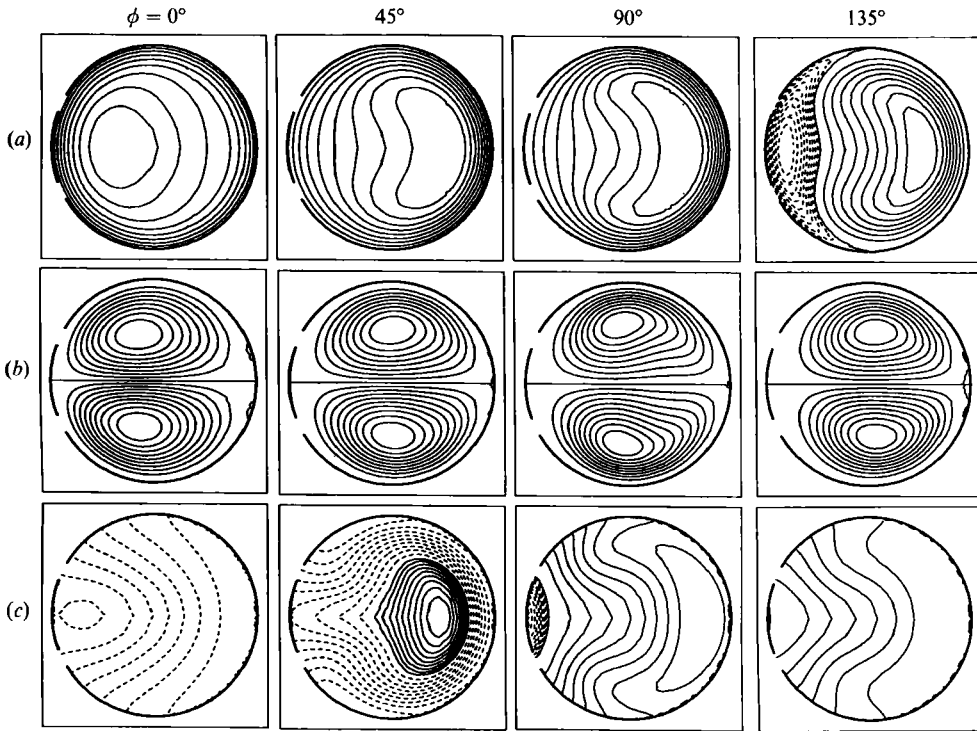


FIGURE 9. Contour plots showing the spectral-element results for different phase angles, ϕ . $\beta^2 = 10$, $Dn = 75.5$, $Dn^2/\alpha^4 = 26.4$. See caption of figure 8 for detailed description.

The point of maximum concentration generally follows the point of maximum axial velocity. In fact, there is reasonable resemblance between the axial velocity contours and concentration isopleths for all phases and all values of Dn . This is in contrast to a previous study of dispersion (Johnson & Kamm 1986) that demonstrated an alignment between the concentration isopleths and the secondary flow streamlines at similar values of Dn^2Sc , but for high Sc and low α . The explanation for the difference is that Johnson & Kamm examined the transition from diffusive to convective dispersion in viscous-dominated flow (zone 1–4), while the present results represent the emerging effects of secondary convection in flow with both viscous and unsteady character and dispersion with both diffusive and unsteady character (zone 1/3 – zone 5/3). This unsteadiness, which can be seen readily in the axial velocity and concentration contours and to a lesser degree in the secondary flow streamlines of figure 9, prevents equilibration of concentration along secondary flow streamlines.

The frequency parameter α for this series is 3.83, close to the lower value of 2.8 employed in the numerical study of Yamane *et al.* (1985). Their results for $Dn = 21.2$ and 212 are quite similar to the present results for $Dn = 33.8$ ($Dn^2Sc = 779$) and $Dn = 75.4$ ($Dn^2Sc = 3876$).

$\beta^2 = 100$ (figures 10 and 11). For these tests, α is sufficiently high to produce a tendency (evident only at the lowest value of Dn) for the two-cell pattern to transform into a four-cell pattern as was previously predicted by Lyne (1971). This tendency, however, is negated once the secondary flow magnitude begins to increase at values of $Dn > 10^2$ and the two-cell pattern reappears. Interestingly, the return of the two-cell pattern produces vortices that are at first highly skewed towards the

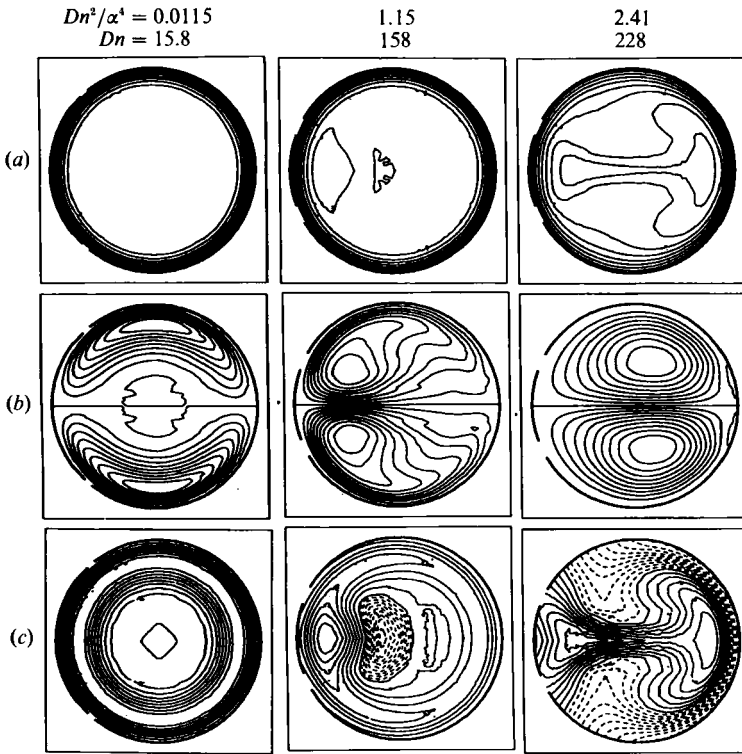


FIGURE 10. Contour plots showing the spectral-element results for different values of Dn . $\beta^2 = 10^2$, $\phi = 90^\circ$. See caption of figure 8 for detailed description.

inside wall (figure 10, $Dn = 158$), before becoming more symmetric again at higher Dn .

The effects of curvature become important when $Dn^2/\alpha^4 \sim O(1)$ (consistent with (2.23)) as evidenced by the changes apparent in the axial velocity and concentration contours. Both clearly exhibit dual peaks for part of the cycle as only suggested in the results for $\beta^2 = 10$. Most critical as far as axial transport is concerned, the axial velocity and concentration gradients become 'smeared' over the entire cross-section, allowing the entire area to take part in the dispersion process rather than restricting it to a narrow boundary layer at the wall as in a straight tube.

The pattern exhibited by the concentration isopleths in figure 11 suggests a region of high concentration circulating around with the secondary flow, having a period of circulation comparable to the cycle period. This coincidence of the secondary flow time and oscillation period was shown in §2 to give rise to enhanced axial transport by a mechanism termed 'convective resonance'. The situation is clouded here, however, because, for $Sc \approx 1$, momentum and mass are similarly affected and the axial velocity peak also tends to move across the tube. Since regions of high axial velocity tend to be associated with regions of high concentration even in the absence of convective resonance (see e.g. the cases with no significant secondary flow) this motion of the peak in concentration alone is insufficient to identify the responsible mechanism.

For these runs, the peak flow lags behind the imposed pressure gradient by 82° for all cases. The results of Yamane *et al.* (1985) for $\alpha = 7.9$ with $Dn = 21.2$ and 212 are similar in range and character to those of this series.

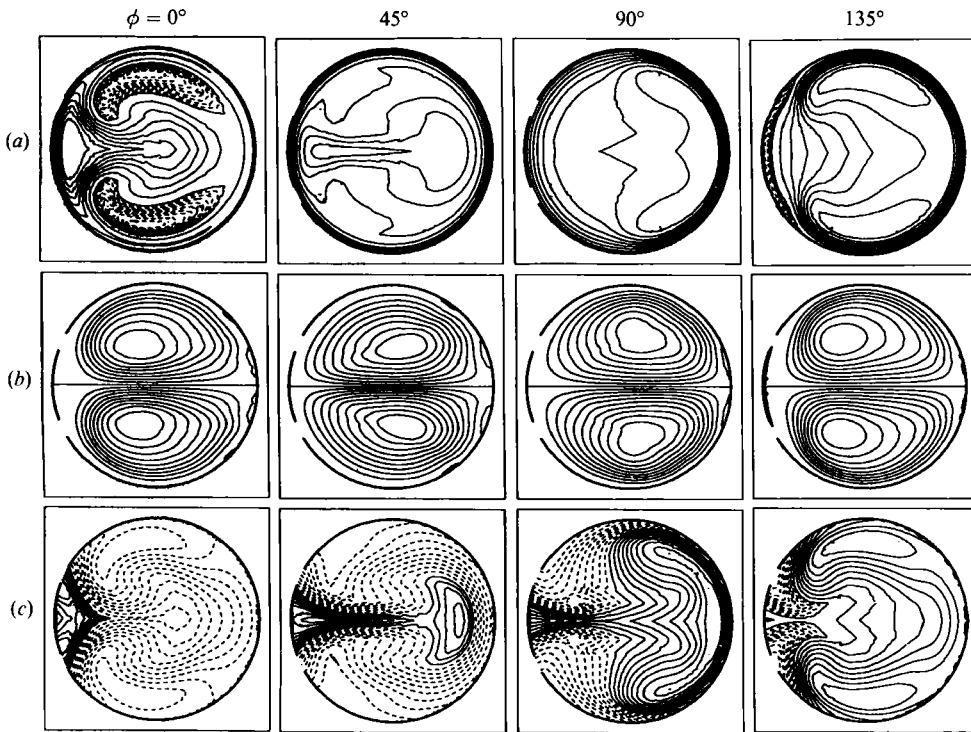


FIGURE 11. Contour plots showing the spectral-element results for different phase angles, ϕ . $\beta^2 = 10^2$, $Dn = 228$, $Dn^2/\alpha^4 = 2.41$. See caption of figure 8 for detailed description.

$\beta^2 = 200$ (figure 12). Of all the conditions tested, this sequence shows best the transition from a four-cell to two-cell pattern as curvature effects come into play. This transition takes place when $Dn^2/\alpha^4 \sim O(1)$, at the point where all curvature effects begin. It is interesting to note that a transition back to a four-cell pattern may occur for high Dn (Daskopoulos & Lenhoff 1989). The flow lags behind the pressure gradient by 84° for both cases.

In this sequence, as in the others at different values of β^2 , it was possible to examine the scaling laws proposed in §2 for variations in the magnitude of the secondary flow velocity, v_s . Consistent with the predictions, $V_s \equiv (v_s/w_0)(b/a)^{1/2}$ was found to vary as Dn for $\alpha < 5$ and as Dn/α^2 for $\alpha > 5$. Furthermore, V_s reached a maximum value ≈ 1 when $Dn > 30$ or when $Dn/\alpha^2 \approx 1$.

6. Discussion and comparison of results

The different transport regimes identified in figure 1 were established in §2 by order-of-magnitude estimates. According to the scaling laws developed there, the effects of curvature on axial transport can be considered negligible in zones 1, 2 and 3. In each case, however, a transition into a zone with significant curvature effects is indicated by a different dimensionless parameter formed by the ratio of the convective term and the dominant term in (2.4) for that zone. In other words, curvature becomes important when the secondary flow time, τ_s , approaches the radial diffusion time, τ_{rd} , for quasi-steady dispersion, or the cycle period, T , for unsteady dispersion. Specifically, when flow and transport are both quasi-steady (zone 1), curvature becomes important when τ_s becomes comparable to τ_{rd} or,

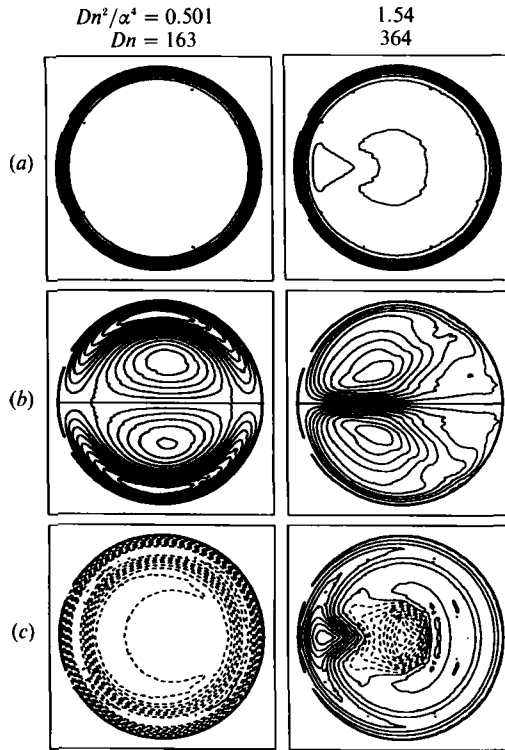


FIGURE 12. Contour plots showing the spectral-element results for different values of Dn . $\beta^2 = 200$, $\phi = 90^\circ$. See caption of figure 8 for detailed description.

equivalently, when the secondary flow Péclet number $Dn^2 Sc \sim O(10^2)$ ((2.18), figures 7*a* and 13*a*). In zone 1, where the flow is quasi-steady, but dispersion is unsteady, secondary flows become significant when τ_s is comparable with T ; or when $Dn^2/\alpha^2 \sim O(10)$ ((2.21) and figure 7*b*). In zone 3 where both flow and transport are unsteady, the transition to significant secondary flow still occurs when $\tau_s/T \sim O(1)$, but since the scaling for v_s , and therefore τ_s , has changed, this occurs when $Dn^2/\alpha^4 \sim O(1)$ ((2.23) and figure 13*b*).

Optimum transport is achieved when the lateral mixing time is comparable with the cycle period, thus the effects of secondary flow manifest themselves in different ways depending on whether radial diffusion is already providing optimal mixing (i.e. whether β^2 is greater or less than 10). For $\beta^2 < 10$, mixing by diffusion is already too rapid, so curvature causes a gradual reduction in \mathcal{D} when $Dn^2 Sc$ increases from $O(10^2)$ to $O(10^5)$, by about a factor of 5 (Johnson & Kamm 1986), to a lower constant value as indicated in figure 7*a* for high Sc . Although the data for $Sc \sim O(1)$ seem to exhibit a similar pattern (figure 13*a*), a separate study in steady flow (Daskopoulos & Lenhoff 1988) has recently shown that \mathcal{D} continues to fall as Dn increases, far below the constant value observed at high Sc . Their results for $Sc = 1$ (also plotted in figure 13*a*) approximately agree with our low- β^2 data for $Sc = 0.68$, but extend to much higher values of Dn . Daskopoulos & Lenhoff (1988) have also shown that when $Dn > 10^2$, a second transition occurs to a regime in which transport rate falls approximately as Dn^{-1} for all Sc . This high- Dn transition has not been observed in previous studies which had used the velocity profiles appropriate for $Dn < 17$. Daskopoulos & Lenhoff attribute this behaviour to a gradual movement of the

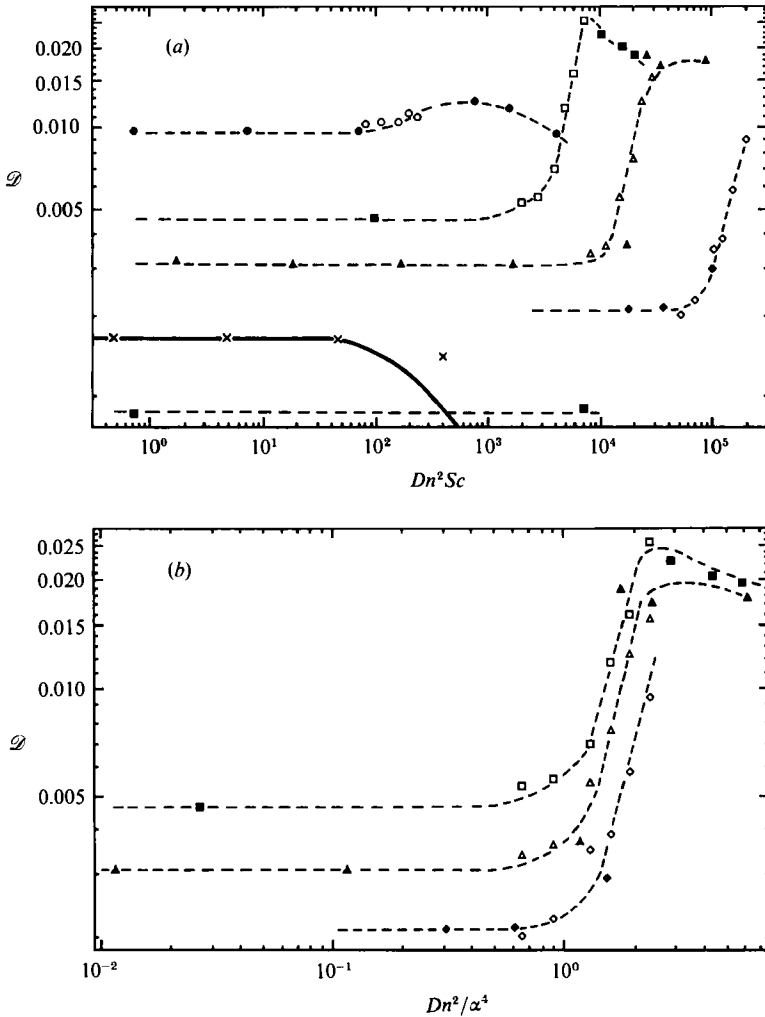


FIGURE 13. Results for axial transport for the spectral-element calculations (fully or partially solid symbols) and selected experimental results (open symbols). (a) \mathcal{D} vs. $Dn^2 Sc$. Values of β^2 are: \times , 1; \bullet , 10; \blacksquare , 50; \blacktriangle , 100; \blacklozenge , 200; \boxplus , 1000 for numerical results; \circ , 9.2; \square , 46; \triangle , 92; \diamond , 230 for the experiments. Solid line is the numerical result of Daskopoulos & Lenhoff (1988). Dashed lines are drawn to fit the present data. (b) \mathcal{D} vs. Dn^2 / α^4 . Symbols as in (a).

secondary flow vortex centre towards the outer wall of the tube and a subsequent reduction in the lateral mixing time.

When $\beta^2 > 10$, increased lateral mixing is beneficial. For $\beta^2 > 10$ and $\alpha < 2$, curvature at first causes an abrupt increase in \mathcal{D} , beginning at $Dn^2 / \alpha^2 \approx 10$ and reaching a peak when $Dn^2 / \alpha^2 \approx 10^2$ (figure 7b). This transport maximum agrees both in location in parameter space and in magnitude with the convective resonance peak observed in a model problem studied by Pedley & Kamm (1988). Although the behaviour beyond the peak cannot be inferred from the present results, scaling predictions (2.21) and (2.22) suggest that \mathcal{D} should eventually scale as β^{-2} as Dn^2 / α^2 is increased further.

When $\beta^2 > 10$ and $Sc \sim O(1)$, the pattern of behaviour is changed only slightly as can be seen by a comparison of figures 7 and 13. As when $Sc \gg 1$, the transition to

a regime influenced by curvature causes an abrupt increase in \mathcal{D} , this time by about a factor of 6, the main difference being that the location of the transition is governed by Dn^2/α^4 rather than by Dn^2/α^2 (figures 7*b* and 13*b*). This pattern was also observed by Eckmann & Grotberg (1987). The appearance of a sharp rise when $\tau_s \sim T$ suggests that convective resonance is again responsible as it was when $Sc \gg 1$. The picture is somewhat complicated in this instance, however, owing to the changing pattern of secondary flow streamlines (figure 11) that produce a form of lateral convective mixing not present in the simulations at high Sc or in the model problem of Pedley & Kamm (1988). Consequently, the transport enhancement observed might be due either to convective resonance or simply to the increase in lateral mixing brought about by the shifting secondary flow pattern. The rate of transport falls slightly as flow amplitude continues to increase but, owing to numerical difficulties, the range of parameters tested beyond the peak is rather small. It is interesting to note, however quite speculatively, that the numerical problems, which are characterized by a gradual appearance of apparently random fluctuations, occur at about the same point at which turbulence was observed in the experiments, despite the two-dimensional nature of the calculation.

Also shown in figure 13 are selected experimental results at values of β^2 that roughly coincide with those chosen for the numerical runs. The experiments fall in the vicinity of the abrupt increase in transport rate and are in generally good agreement with the computed results.

7. Comments on pulmonary gas transport

In recent experiments (Paloski, Slosberg & Kamm 1987), it was found that axial transport rate in a lung-like model was about a factor of 3 greater than that in a straight tube of similar dimensions, independent of the stroke volume and frequency combination used. At high β^2 , the results reported here for a uniformly curved tube also exhibit a relatively constant increase in \mathcal{D} , by about a factor of 6 provided that $Dn^2/\alpha^4 \gtrsim 2$.

This comparison and the recognition that secondary flows of the type seen in curved tubes are also observed in lung-like models (Schroter & Sudlow 1969) provide some basis for applying the present results to mechanical ventilation of the lung. When $Sc \approx 1$, as it is for most respiratory gases, figure 1(*b*) pertains and zones 2 and 4 are eliminated. Therefore, \mathcal{D} is reduced by secondary flow for $\beta^2 < 10$ when Dn^2Sc rises above $O(10^2)$, but is enhanced for $\beta^2 > 10$ when Dn^2/α^4 (which is proportional to the square of the axial stroke length) exceeds $O(1)$. Under typical flow conditions used in high-frequency oscillation, only in the trachea and first several generations in the lung is $\beta^2 > 10$ (Jan, Shapiro & Kamm 1989). The rest of the airways fall into the low- β^2 regime by virtue of their small dimension. Furthermore, the nature of the branching geometry causes the normalized stroke length (and therefore Dn^2/α^4) to be relatively invariant over the entire network thereby leading to a locus of states existing in the lung that lie along a line parallel to the zone 3–5*c* boundary for a given frequency and tidal volume. Keeping in mind that the rate of gas transport will vary as $D_{\text{eff}} = w_0^2 T \mathcal{D}$, two possibilities for optimization suggest themselves. Noting that the pressures generated in the lung, and therefore the potential for lung damage and cardiovascular complications, increase with increasing flow velocity and frequency, there may be some advantage in choosing a value of Dn^2/α^4 just large enough to attain the high rates of dispersion of zone 5*c* in the large airways, but not so high as to bring about the reduced transport associated with zone 5*a* in the small to medium

sized airways. On the other hand, if that flow condition proves incapable of producing adequate gas exchange (as seems likely based on previous animal experiments (Drazen *et al.* 1984)) the alternative is to simply boost stroke volume and frequency, with the emphasis being on stroke volume.

8. Summary

The behaviour of axial transport has been studied and characterized for a wide range of oscillatory flow conditions in a uniform tube with small curvature ratio. A variety of methods have been employed including two numerical procedures and a series of experiments. Several regions of overlap exist and the agreement is generally quite good.

The existence of a sharp increase in transport rate is demonstrated for $\beta^2 > 10$, in liquids when $Dn^2/\alpha^2 \sim O(10^2)$, and in gases when $Dn^2/\alpha^4 \sim O(1)$. Peaks occur when $\tau_s \sim T$, suggesting that they are caused by a type of resonance phenomenon.

The calculated flow patterns for Dn^2/α^4 both above and below 1 illustrate a transition from the four-cell pattern observed in numerous previous studies, to a two-cell pattern characteristic of lower values of α^2 . The four-cell pattern appears to be stable only when the secondary flow is incapable of producing significant mixing in the cross-sectional plane.

These findings suggest that, to the extent that transport in the airways of the lung is influenced by the curvature found in each bifurcation, the rate of axial gas exchange can be enhanced by operating at frequencies and tidal volumes which produce local values of $Dn^2/\alpha^4 > 1$ throughout the lung.

The support of the National Science Foundation (8313017-MEA) and the National Institutes of Health (HL33009) are gratefully acknowledged. The spectral-element calculations were performed using a modified version of NEKTON (Nektonics, Inc., Cambridge, MA 02134).

Appendix. Spectral-element method

The normalized mass momentum and species conservation equations ((2.1)–(2.4)) are solved numerically in domain D with boundary ∂D . A mixed explicit–implicit time advancement splitting scheme is employed for the temporal discretization similar to the scheme first used by Orszag & Kells (1980). The advantage of the scheme is that it reduces the coupled system of momentum equations into separately solvable equations for pressure and velocity. The axial momentum equation is solved first, beginning with a third-order Adams–Bashforth formulation for the nonlinear terms,

$$\frac{\hat{w}^{n+1} - w^n}{\Delta t} = - \sum_{k=0}^2 \beta_k (\mathbf{v}^{n-k} \cdot \nabla w^{n-k}) + \Pi_z^{n+\frac{1}{2}} \quad \text{in } D, \quad (\text{A } 1)$$

where $\beta_0 = 23/13$, $\beta_1 = -16/12$ and $\beta_2 = 5/12$ and $w^n = w(n\Delta t)$, $\mathbf{v}^n = \mathbf{v}(n\Delta t)$ and $\Pi_z^{n+\frac{1}{2}} = \Pi_z[(n+\frac{1}{2})\Delta t]$. This is followed by the implicit viscous correction step (Crank–Nicolson)

$$\frac{w^{n+1} - \hat{w}^{n+1}}{\Delta t} = \frac{2}{Dn} \nabla^2 [\frac{1}{2}w^{n+1} + \frac{1}{2}w^n] \quad \text{in } D; \quad (\text{A } 2)$$

the no-slip boundary conditions for w are imposed at this step. The cross-sectional momentum equations are solved next using

$$\frac{\hat{v}^{n+1} - v^n}{\Delta t} = \sum_{k=0}^2 \beta_k [v^{n-k} \times \omega^{n-k}], \quad (\text{A } 3)$$

where $\omega^n = \nabla \times v^n$ is the vorticity. Continuity is satisfied in the pressure step by an equation formed by taking the divergence of the cross-sectional momentum equations and including the continuity constraint, for the intermediate velocity component \hat{v} , i.e. $\nabla \cdot \hat{v} = 0$,

$$\nabla^2 \Pi' = \nabla \cdot \frac{\hat{v}^{n+1}}{\Delta t}, \quad (\text{A } 4)$$

$$\frac{\hat{v}^{n+1} - \hat{v}^{n+1}}{\Delta t} = -\nabla \Pi', \quad (\text{A } 5)$$

both applied in domain D . The boundary condition for pressure is of Neumann type and is derived from (A 5) by further assuming that $\hat{v} \cdot n = 0$ (n is the unit vector normal to the boundary):

$$\frac{\partial \Pi'}{\partial n} = \frac{\hat{v}^{n+1} \cdot n}{\Delta t}.$$

The viscous correction step is given by

$$\frac{v^{n+1} - \hat{v}^{n+1}}{\Delta t} = \frac{2}{Dn} \nabla^2 [\frac{1}{2}v^{n+1} + \frac{1}{2}\hat{v}^{n+1}]. \quad (\text{A } 6)$$

Lastly, the species conservation equation is also solved in two substeps as follows:

$$\frac{\hat{C}^{n+1} - C^n}{\Delta t} = \sum_{k=0}^2 \beta_k v^{n-k} \cdot \nabla C^{n-k} - w^{n+\frac{1}{2}} G, \quad (\text{A } 7)$$

$$\frac{C^{n+1} - \hat{C}^{n+1}}{\Delta t} = \frac{2}{DnSc} [\frac{1}{2}C^{n+1} + \frac{1}{2}C^n] \quad \text{in } D, \quad (\text{A } 8)$$

with
$$\nabla C \cdot n = 0 \quad \text{on } \partial D \quad (\text{A } 9)$$

employed in substep (A 8).

Equations (A 1), (A 3) and (A 7) represent explicit treatment of the convective terms. We choose the Adams–Bashforth third-order method because of its very low dispersion errors and the relatively large portion of the imaginary axis included within the absolute stability region of the scheme. The implicit treatment of the diffusive contributions in (A 2), (A 6) and (A 8) results in a very efficient and robust inversion of the global system matrices. The time step is dictated by (A 1), (A 3) and (A 7) and time-accuracy considerations. The scheme overall has $O(\Delta t)$ accuracy, although all intermediate substeps involve high-order integration schemes.

The spatial discretization is performed using an isoparametric spectral-element method (Patera 1984), a high-order weighted-residual technique which combines the flexibility of finite-element methods (Strang & Fix 1973) and the accuracy of spectral schemes (Gottlieb & Orszag 1977). The domain D is divided into quadrilateral elements with local coordinates (r, s) which map to global space (x, y) by tensor product mapping

$$(x, y)_N^k = \sum_{i=0}^N \sum_{j=0}^N (x, y)_{ij}^k h_i(r) h_j(s), \quad (\text{A } 10)$$

and the dependent variables are described by

$$f_N^k = \sum_{i=0}^N \sum_{j=0}^N f_{ij}^k h_i(r) h_j(s). \quad (\text{A } 11)$$

For convenience the resolution in the two spatial directions has been assumed to be the same; however, in practice this need not be the case. Here $(x, y)_{ij}^k$ represents the global coordinates of grid points within element k , and the f_{ij}^k are the nodal values of dependent variables f_n^k . The $h_m(q)$ are N th-order local Chebyshev–Lagrangian interpolants, which have the property

$$h_m(q_n) = \delta_{mn},$$

where δ_{mn} is the Kronecker delta. This is the generalized procedure for finite-element tensor product bases, where $N = 1$ gives the common case of bilinear interpolants,

$$h_0(q) = \frac{1}{2}(1-q), \quad h_1(q) = \frac{1}{2}(1+q). \quad (\text{A } 12)$$

In extending this procedure to higher order, collocation points (nodal points within the element) are chosen on a Gauss–Lobatto–Chebyshev distribution in local coordinate q_n :

$$q_n = -\cos\left[\frac{\pi n}{N}\right], \quad n = 0, N$$

to assure rapid convergence (Gottlieb & Orszag 1977).

The matrix from the discretized equation is obtained by substituting (A 10) and (A 11) into the variational equivalent of the governing equations and selecting test functions identical to the high-order extension of (A 12). Implementation details are discussed in Korczak & Patera (1986) and Karniadakis (1990). Similar spectral-element codes have been validated with experimental results in a variety of unsteady laminar as well as turbulent flows (Karniadakis 1989).

REFERENCES

- BERGER, S. A., TALBOT, L. & YAO, L. S. 1983 Flow in curved pipes. *Ann. Rev. Fluid Mech.* **15**, 461–512.
- CRANK, J. 1956 *The Mathematics of Diffusion*, p. 147. Clarendon.
- DASKOPOULOS, P. & LENHOFF, A. J. 1988 Dispersion coefficient for laminar flow in curved tubes. *AIChE J.* **34**, 2052–2058.
- DASKOPOULOS, P. & LENHOFF, A. J. 1989 Flow in curved ducts: bifurcation structure for stationary ducts. *J. Fluid Mech.* **203**, 125–148.
- DEAN, W. R. 1928 The streamline motion of fluid in a curved pipe. *Phil. Mag.* **5** (7), 673–695.
- DRAZEN, J. M., KAMM, R. D. & SLUTSKY, A. S. 1984 High-frequency ventilation. *Physiol. Rev.* **64**, 505–543.
- ECKMANN, D. M. & GROTBORG, J. B. 1987 Oscillatory flow and mass transport in a curved tube. *J. Fluid Mech.* **188**, 509–527.
- ERDOGAN, M. E. & CHATWIN, P. C. 1967 The effects of curvature and buoyancy on the laminar dispersion of solute in a horizontal tube. *J. Fluid Mech.* **29**, 465–484.
- FISCHER, H. B. 1972 Mass transport mechanisms in partially stratified estuaries. *J. Fluid Mech.* **53**, 671–687.
- GOTTLIEB, G. O. & ORSZAG, S. A. 1977 *Numerical Analysis of Spectral Methods: Theory and Application*. NSF-GBMS Monograph, No. 26. SIAM.
- HINO, M., SAWAMOTO, M. & TAKASU, S. 1976 Experiments on transition to turbulence in an oscillatory pipe flow. *J. Fluid Mech.* **75**, 193–207.

- HOLLEY, E. R., HARLEMAN, D. R. F. & FISCHER, H. B. 1970 Dispersion in homogeneous estuary flow. *J. Hydraul. Engng Div. ASCE* **96**, 1691–1709.
- JAN, D. L., SHAPIRO, A. H. & KAMM, R. D. 1989 Some features of oscillatory flow in a model bifurcation. *J. Appl. Physiol.* **67**, 147–159.
- JANSSSEN, L. A. M. 1976 Axial dispersion in laminar flow through coiled tubes. *Chem. Engng Sci.* **31**, 215–218.
- JOHNSON, M. & KAMM, R. D. 1986 Numerical studies of steady flow dispersion at low Dean number in a gently curving tube. *J. Fluid Mech.* **172**, 329–345.
- JOSHI, C. H., KAMM, R. D., DRAZEN, J. M. & SLUTSKY, A. S. 1983 An experimental study of gas exchange in laminar oscillatory flow. *J. Fluid Mech.* **133**, 245–254.
- KARNIADAKIS, G. E. 1989 Spectral element simulations of laminar and turbulent flows in complex geometries. *Appl. Numer. Math.* **6**, 85–105.
- KORCZAK, K. Z. & PATERA, A. T. 1986 An isoparametric spectral element method for solution of the Navier–Stokes equations in complex geometry. *J. Comput. Phys.* **62**, 361–382.
- KURZWEIG, U. H. 1985 Enhanced heat conduction in fluids subjected to sinusoidal oscillations. *Trans. ASME C: J. Heat Transfer* **107**, 459–462.
- LYNE, W. H. 1971 Unsteady viscous flow in a curved pipe. *J. Fluid Mech.* **45**, 13–31.
- NUNGE, R. J., LIN, T.-S. & GILL, N. 1972 Laminar dispersion in curved tubes and channels. *J. Fluid Mech.* **51**, 363–383.
- ORSZAG, S. A. & KELLS, L. C. 1980 Transition to turbulence in plane Poiseuille flow and plane Couette flow. *J. Fluid Mech.* **96**, 159–205.
- PALOSKI, W. H., SLOSBERG, R. B. & KAMM, R. D. 1987 Effects of gas properties and waveform asymmetry on gas transport in a branching tube network. *J. Appl. Physiol.* **63**, 892–902.
- PATERA, A. T. 1984 A spectral element method for fluid dynamics: laminar flow in a channel expansion. *J. Comput. Phys.* **54**, 468–488.
- PEDLEY, T. J. 1980 *The Fluid Mechanics of Large Blood Vessels*, pp. 160–234. Cambridge University Press.
- PEDLEY, T. J. & KAMM, R. D. 1988 The effect of secondary motion on axial transport in oscillatory tube flow. *J. Fluid Mech.* **193**, 347–367.
- RHINES, P. B. & YOUNG, W. R. 1983 How rapidly is a passive scalar mixed within closed streamlines? *J. Fluid Mech.* **133**, 133–145.
- SCHROTER, R. C. & SUDLOW, M. F. 1969 Flow patterns in models of the human branchial airways. *Respir. Physiol.* **7**, 341–355.
- SHARP, M. K. 1987 Dispersion in a curved tube during oscillatory flow. Sc.D. thesis, Department of Mechanical Engineering, MIT.
- SMITH, R. 1982 Contaminant dispersion in oscillatory flows. *J. Fluid Mech.* **114**, 379–398.
- SREENIVASAN, K. R. & STRYKOWSKI, P. J. 1983 Stabilization effects in flow through helically coiled pipes. *Expts Fluids* **1**, 31–36.
- STRANG, G. & FIX, G. J. 1973 *An Analysis of the Finite Element Method*. Prentice-Hall.
- TAYLOR, G. I. 1921 Diffusion by continuous movements. *Proc. Lond. Math. Soc.* **20** (2), 196–212.
- TAYLOR, G. I. 1953 Dispersion of soluble matter in solvent flowing slowly through a tube. *Proc. R. Soc. Lond. A* **219**, 186–203.
- TOPAKOGLU, H. C. 1967 Steady laminar flows of an incompressible viscous fluid in curved pipes. *J. Math. Mech.* **16**, 1321–1337.
- WATSON, E. J. 1983 Diffusion in oscillatory pipe flow. *J. Fluid Mech.* **133**, 233–244.
- YAMANE, R., OSHIMA, S., SUDO, K., SUMIDA, M., OKAMOTO, N. & KIZAKI, M. 1985 Study of oscillatory flow in curved channel. *Bull. JSME* **28**, 428–435.
- YOUNG, W. R., RHINES, P. B. & GARRETT, C. J. 1982 Shear-flow dispersion, internal waves and horizontal mixing in the ocean. *J. Phys. Oceanogr.* **12**, 515–527.